IEICE TRANS. INF. & SYST., VOL.E93–D, NO.10 OCTOBER 2010

PAPER

Phase Portrait Analysis for Multiresolution Generalized Gradient Vector Flow

Sirikan CHUCHERD[†a)], ***Member***, **Annupan RODTOOK**[††], ***and*** **Stanislav S. MAKHANOV**[†], ***Nonmembers***

SUMMARY We propose a modification of the generalized gradient vector flow field techniques based on multiresolution analysis and phase portrait techniques. The original image is subjected to mutliresolutional analysis to create a sequence of approximation and detail images. The approximations are converted into an edge map and subsequently into a gradient field subjected to the generalized gradient vector flow transformation. The procedure removes noise and extends large gradients. At every iteration the algorithm obtains a new, improved vector field being filtered using the phase portrait analysis. The phase portrait is applied to a window with a variable size to find possible boundary points and the noise. As opposed to previous phase portrait techniques based on binary rules our method generates a continuous adjustable score. The score is a function of the eigenvalues of the corresponding linearized system of ordinary differential equations. The salient feature of the method is continuity: when the score is high it is likely to be the noisy part of the image, but when the score is low it is likely to be the boundary of the object. The score is used by a filter applied to the original image. In the neighbourhood of the points with a high score the gray level is smoothed whereas at the boundary points the gray level is increased. Next, a new gradient field is generated and the result is incorporated into the iterative gradient vector flow iterations. This approach combined with multiresolutional analysis leads to robust segmentations with an impressive improvement of the accuracy. Our numerical experiments with synthetic and real medical ultrasound images show that the proposed technique outperforms the conventional gradient vector flow method even when the filters and the multiresolution are applied in the same fashion. Finally, we show that the proposed algorithm allows the initial contour to be much farther from the actual boundary than possible with the conventional methods.

key words: *phase portrait analysis, multiresolution analysis, medical image processing*

1. Introduction

Among the most promising techniques for extraction of complex objects from digital images are active contours or snakes, originally introduced by Kass et al. [1]. The snakes have been used to locate the object boundaries in various applications of medical image processing with a different degree of success. In particular, they have been successfully applied to segmentation of abnormalities in the images of the human heart, liver, brain, breast, etc [2]–[12].

A variety of improvements to Kass's method have been proposed [13], [14], where edge-based external forces, enhancing the effect of image edges have been introduced to overcome the sensitivity to the initial conditions and the noise.

The so-called T-snakes [15] and their improvements such as the dual T-snakes models [16] are able to reparameterize the snakes and use multiple contours. An intrinsic internal force based on regularized contour curvature profile was introduced in [17] and [18]. A grammatical framework [19] presents different local energy models and a set of allowable transitions between these models. The sectored snakes [20] deform the contour under constraints derived from a priori knowledge of the object shape. Fourier snakes [21] evolve to a prescribed shape defined by a template. Region-based image features are combined with the edge-based features incorporated in the external forces [22], [23]. The snake based segmentation can be also performed starting from multiple seeds by iterative boundary deformation and region merging [24].

A competing approach called the level set method [25] is based on the ideas proposed by Osher and Sethian [26] to use a model of propagating liquid interfaces with curvature-dependent speeds.

The level set method combined with the contour energy minimization resulted in a variety of the so-called geodesic deformable models [27]–[31]. Siddiqi et al. [28] incorporate an area function and the edge function into the length minimization framework to strengthen the contour attracting force. Rochery et al. [32] proposed a parametric model for higher-order active contours, in particular, quadratic snakes, for extraction of linear structures like roads. However, the level set representation makes it difficult to impose arbitrary geometric or topological constraints on the evolving contour via the higher dimensional hyper surface [15]. Besides, the level set models may generate shapes having inconsistent topology with respect to the actual object, when applied to noisy images characterized by large boundary gaps [33] requiring exhaustive optimization to accomplish reasonable run times [34].

Further improvements lie along the lines of processing the underlying vector field rather than modifying the snake model itself. A number of popular codes are based on a gradient vector flow (GVF) method proposed by Prince and Xu [35], [36]. A "raw" gradient vector field derived from the image edges is replaced by a vector field which minimizes a certain variational functional. The functional is designed

Manuscript received December 15, 2009.
Manuscript revised May 17, 2010.

[†]The authors are with the School of Information, Computer and Communication Technology, Sirindhorn International Institute of Technology, Thammasat University, Bangkadi Campus, Pathum Thani 12000, Thailand.

[††]The author is with the Computer Science Department, Ramkhamhaeng University, Bangkok 10240, Thailand.

a) E-mail: D5022300015@studentmail.siit.tu.ac.th

DOI: 10.1587/transinf.E93.D.2822

to extend the large gradients far from the boundary, smooth the gradients caused by noise and speckles while keeping gradients attached to strong edges. The generalized gradient vector flow field (GGVF) [37] extends GVF by introducing an analogy with non-uniform diffusion. Some variations of this idea are given in [38], [39].

The GGVF-preprocessed images often allow the snakes to avoid gradients produced by the speckles and the tissue-related edges. However, when the noise related gradients are comparable with the boundary gradients, the diffusion smoothes the false and the true contour points equally. Although on average GGVF produces a smoother vector field it may also lead to undesirable effects nearby concave boundaries. Besides it may generate such unwanted configurations as the attracting or the repelling stars. In this paper, we propose a special numerical treatment of the GGVF equations to improve the accuracy and convergence of the snake subjected to the resulting vector field. Our modification called phase portrait orientation force field analysis (PPA) inspired by discrete force field analysis proposed in [40] uses intermediate vector fields obtained during the numerical iterations to construct an improved edge map.

PPA is based on a numerical measure of a strong edge, applied in a rotating window of a varying size. This part of the algorithm is similar to oriented filtering (the oriented Gabor filter, the oriented LoG filter, etc). However, the proposed method differs from the conventional filters. PPA produces a score which measures the similarity of the vector field in the particular window to the boundary pattern. The boundary configuration is represented by the attractive or repelling line (node saddle case I and II, see Fig. 1) characterized by certain eigenvalues of the corresponding linear flow matrix. The noise is represented by the attracting and the repelling nodes or stars (see Fig. 1). Since the gradient vector field is rotation-free, the local flow is limited to above patterns whereas patterns like "focus" or "center" do not appear.

The idea of using the phase portrait for image analysis is not new (see, for instance [41]). It has been applied to the fingerprint identification [42]–[44], texture analysis [45], satellite imagery [46], [47] and many other image processing applications. In particular the phase portrait techniques have been applied to detect architectural distortions in mammogram breast images [48]. However, to the best of our knowledge the phase portrait analysis has not been applied in a context of multiresolution active contours for generation of improved edge maps. Besides, as opposed to the majority of the phase portrait techniques based on "if-then" rules, we propose a continuous measure derived from the corresponding vector flow matrix.

The continuous measure makes it possible to adapt the edge map at each resolution level to obtain an improved GGVF. The approach has been tested using synthetic low contrast images. It offers a simple computational scheme and leads to a higher segmentation accuracy. Our numerical experiments on numerous images show similar or better accuracy but at the same time much less sensitivity to the snake controlling parameters and the initial position of the contour as compared with the conventional GGVF, multiresolution GGVF snakes and multiresolution snakes endowed with conventional filters. Finally, our numerical experiments with medical ultra-sound breast tumor images show that the proposed method is more appropriate than the above mentioned methods as applied to segmentation of the breast tumors.

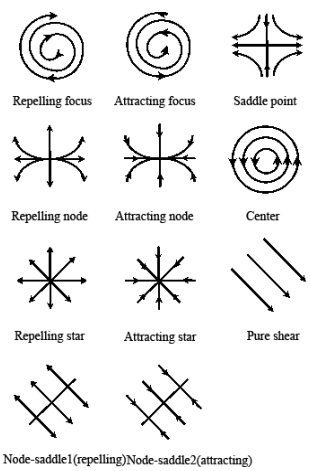

Fig. 1 Phase portrait flow pattern.

2. Snakes in the Framework of the Gradient Vector Flow Technique

An active contour or snake parametrically defined as $X(s) = (x(s), y(s))$, $s \in [0, 1]$ is a curve which evolves inside the image domain so that it attaches itself to the desired object. The evolution of the snake is governed by Euler equations corresponding to an energy functional defined by

$$E = \int_0^1 \frac{1}{2}\left(a\left|X'(s)\right|^2 + b\left|X''(s)\right|^2\right) ds + \int_0^1 E_{\text{ext}}(X(s))\, ds, \tag{1}$$

where E_{ext} is an external force which moves the snake towards the object, for instance, it could be a smoothed version of the gradient vector field. The minimum of the functional is supposed to be a curve which approximates a boundary of the object of interest. Although this claim has not been proven theoretically for realistic assumptions such as the presence of noise, false objects, speckles, low contrast areas etc, a strong rationale behind it is variational functional (1).

Popular gradient vector flow techniques (GVF) originally proposed by Prince and Xu [35], [36], replaces a "raw" gradient vector field $E_{\text{ext}}(X(s))$ derived from the image edges by a new vector field. The vector field is obtained by extending the large gradients far from the boundary and smoothing the gradients caused by noise. The GVF is a minimizer of the following functional

$$\mu \iint |\nabla u|^2 + |\nabla v|^2 \, dx\, dy + \iint |\nabla f|^2 |V - \nabla f|^2 \, dx\, dy, \quad (2)$$

where μ is the diffusion coefficient.

The first integral produces a smoothly varying vector field $V = (u(x, y), v(x, y))$, while the second integral encourages the vector field to approach ∇f, if $|\nabla f|$ is large.

The Euler equation for functional (2) is given by

$$\mu \nabla^2 V - (V - \nabla f)|\nabla f|^2 = 0, \quad (3)$$

Equation (3) can be solved by treating V as a function of time and solving

$$\frac{\partial V}{\partial t} = \mu \nabla^2 V - (V - \nabla f)|\nabla f|^2. \quad (4)$$

The steady-state solution (as $t \to \infty$) of the linear parabolic equation above is the desired solution of the Euler equation (3). Equation (4) is discretized with regard to the time and space variables and solved numerically. The time steps are interpreted as numerical iterations.

Furthermore, Xu and Prince [37] extended the GVF technique by introducing spatially varying coefficients to decrease the smoothing effect, namely,

$$\frac{\partial V}{\partial t} - g(|\nabla f|)\nabla^2 V - h(|\nabla f|)(\nabla f - V) = 0. \quad (5)$$

The improved version of the GVF is called the generalized gradient vector flow (GGVF). The weighting functions g and h depend on the gradient of the edge map so that in the proximity of large gradients g gets smaller whereas h becomes larger. In [37] the following weighting functions have been proposed

$$g(|\nabla f|) = e^{-(|\nabla f|/K)}, \; h(|\nabla f|) = 1 - g(|\nabla f|), \quad (6)$$

where K is a calibration parameter.

However, the GVF may produce a vector field, where the gradients are not extended far enough from the actual boundary of the object. On the other hand, the true boundary can be partially or even entirely destroyed by excessive smoothing when μ or the time step are too large.

The smoothing effect depends on the diffusion coefficient μ (or K in case of (6)) and the iteration step. If a conventional stopping criteria based on the proximity to the steady state solution produces an "over-smoothed" solution, the user must modify the diffusion coefficient or interrupt the iterations earlier. However, interrupting the iterations too early may lead to false boundaries and artifacts.

The proposed PPA treats this problem by using local configurations of the vector field. If the local pattern resembles the noise the algorithm applies additional smoothing. If PPA detects a possible boundary the smoothing (diffusion) becomes small, so that this part of the vector field remains unchanged. Our experiments show, that the same set of parameters produces a much better accuracy when PPA is applied. As a matter of fact, since PPA adapts the diffusion automatically, it is often the case that the dependence of the accuracy on K is substantially reduced.

3. Orientation Force Field Analysis and Phase Portrait Techniques

The main idea of the discrete orientation force field analysis (DOFFA) proposed by Hou and Han [40] is that the true boundary vectors must face each other along a certain direction. Therefore, DOFFA introduces a 3×3 sampling window around the candidate boundary point and analyses the directions of the vector field in this window. This procedure is illustrated in Fig. 2.

Positions (1)–(4) and sixteen positions (5)–(8) (including rotations and the symmetric positions) in Fig. 2 constitute the basic configuration of DOFFA. However, DOFFA introduces many other positions such as the broken point (9), (10) and others. It is not clear whether the set of the positions is complete. Of course, for the real image the vectors are not precisely anti-parallel. Therefore, the definition of approximately anti parallel vectors must be based on a certain threshold of the angle between the vectors. This threshold is often hard to find.

Furthermore, the major drawback of DOFFA is that it is hard to extend to large windows. Even for a window 5×5 possible boundary configurations are hard to introduce and interpret.

In this paper, we introduce a modification of DOFFA based on phase portrait analysis combined with wavelet multiresolution analysis (filter bank).

The phase portrait analysis makes it possible to introduce a continuous measure indicating the boundary point, regular point or noise based on the eigenvalues of the linear flow matrix. The method applies to any size of the sampling window and works well combined with GGVF iterations.

Recall that the linear system model represents the underlying vector field V as a solution of a linear system $\frac{dv}{dt} = Av$. Matrix $A = \begin{pmatrix} a & b \\ c & d \end{pmatrix}$ can be obtained by a linear least square method applied in the sampling window to minimize $\|V - A\begin{pmatrix} x \\ y \end{pmatrix}\|$ with regard to a, b, c and d.

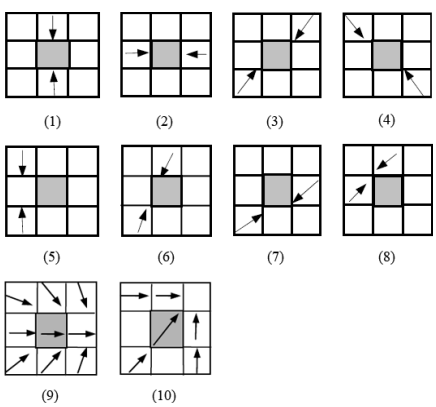

Fig. 2 Basic vector configurations for the discrete orientation force field analysis (DOFFA).

Table 1 Types of 2D critical points.

Pattern	Eigenvalues	
Center	$R_1 = R_2 = 0$	$I_1 = -I_2 \neq 0$
Attracting Focus	$R_1 = R_2 < 0$	$I_1 = -I_2 \neq 0$
Repelling Focus	$R_1 = R_2 > 0$	$I_1 = -I_2 \neq 0$
Attracting Node	$R_1 \neq R_2 < 0$	$I_1 = I_2 = 0$
Attracting Star	$R_1 = R_2 < 0$	$I_1 = I_2 = 0$
Repelling Node	$R_1 \neq R_2 > 0$	$I_1 = I_2 = 0$
Repelling Star	$R_1 = R_2 > 0$	$I_1 = I_2 = 0$
Saddle Point	$R_1 > 0, R_2 < 0$	$I_1 = I_2 = 0$
Node-Saddle 1	$R_1 > 0, R_2 = 0$	$I_1 = I_2 = 0$
Node-Saddle 2	$R_1 < 0, R_2 = 0$	$I_1 = I_2 = 0$
Pure Shear	$R_1 = R_2 = 0$	$I_1 = I_2 = 0$

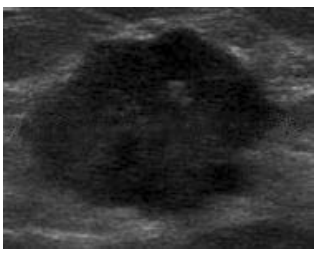

Fig. 3 Ultrasound breast tumor image.

There are eleven basic linear flow patterns characterized by the eigenvalues of matrix A (see Table 1 [49], where λ_1, λ_2 are the eigenvalues, $R_i = \mathrm{Re}\lambda_i$, $I_i = \mathrm{Im}\lambda_i$ see also Fig. 1). Since we apply our classification to the vector field subjected to smoothing and boundary enhancing effects of GGVF. The most prominent patterns are attracting/repelling stars (noise), node-saddle (boundary) and the pure share (regular point). These configurations can be explained considering a physical analogy of the heat diffusion simulated by Eq. (4) and the resulting vector field. It is clear that the noise generates an isolated source (sink) of heat. In terms of the corresponding vector field it is an attracting (repelling) star. In turn, a boundary of the object corresponds to a source (sink) distributed along the corresponding curve. In this case PPA detects an attracting or repelling node-saddle. Finally, a slow varying gray level (background) corresponds to "shear".

Consider the case of ultrasound breast tumor images. The tumors are represented by dark spots at the lighter noisy background (see Fig. 3). Usually, the tumor also includes, small and large group of lighter pixels representing noise. The boundary of the tumor is typically ill-defined, fuzzy and is often hard to evaluate visually. In this case the most frequent patterns are: attracting star, attracting saddle node (boundary) and the shear (a regular point).

Our classifier is given by

$$C(W) = \begin{cases} \text{noise}, \ \frac{\min(|\lambda_1|,|\lambda_2|)}{\max(|\lambda_1|,|\lambda_2|)} > \Delta_1, \\ \quad |\lambda_1| > \Delta_2 \ \text{or} |\lambda_2| > \Delta_2 \\ \text{boundary}, \ \frac{\min(|\lambda_1|,|\lambda_2|)}{\max(|\lambda_1|,|\lambda_2|)} \leq \Delta_1, \\ \quad |\lambda_1| > \Delta_2 \ \text{or} |\lambda_2| > \Delta_2 \\ \text{regular point}, \\ \quad |\lambda_1| \leq \Delta_2 \ \text{or} |\lambda_2| \leq \Delta_2 \end{cases} \tag{7}$$

where W is the window around the pixel and Δ_1, Δ_2 the thresholds evaluated by training. The classifier runs for various sizes of the window in increasing order.

Finally, the edge map used to iteratively apply the GGVF is modified as follows. If $C(W)$ = "noise", then the corresponding window gets smoothed by an appropriate filter, if $C(W)$ = "boundary", the gray level of the edge map gets increased. Finally, if $C(W)$ = "regular point", the gray level remains the same. The entire iterative algorithm is presented in the next section.

4. Iterative Algorithm

The algorithm is based on the above GGVF -PPA snake combined with multiresolution analysis (MRA) or filter bank. The filter bank is based on the Daubechies wavelets D4 [50]. The number of the multiresolution levels is hand-tuned for the best performance. Typically 2-3 multiresolution levels are required.

The PPA classifier detects the noise and the boundary points for each multiresolution level and for various sizes of the window in increasing order. The snake runs at each multiresolution level and is then interpolated to the next level. This part of the algorithm is similar to [51], [52]. PPA detects the boundary points, noise and the regular points. The first run of PPA removes the noise with an increasing size of sampling windows. The second run detects the boundary. If the point belongs to the boundary the gray level in the central point gets increased. The gradient vector field ∇f is then reconstructed and GGVF applies to the improved ∇f. Finally, the snake runs on the resulting vectors field until convergence. The procedure is repeated on each resolution level.

The proposed algorithm called GGVF-MRA-PPA snake consists of the following steps.

1. Apply MRA (Daubechies-D4) to the original image.
2. Set the resolution level to the lowest one.
3. Apply the Canny edge detector to obtain a gray level edge map.
4. Evaluate ∇f.
5. Noise removal step:
   - 5.1 Apply the PPA with a certain window size to obtain $C(W)$ at every point.
   - 5.2 If $C(W)$ = "noise" smooth the gray level map at this window.
   - 5.3 Increase the size of the window and go to 5.1 until the maximum allowed window size is reached.
6. Evaluate new ∇f.
7. Edge detection step:
   - 7.1 Apply PPA with a certain window size to obtain $C(W)$ at every point.
   - 7.2 If $C(W)$ = "boundary", increase the gray level of the edge map and exclude this point from further runs.

7.3 Increase the size of the window and go to 7.1 until the maximum window size is reached.

8. Evaluate new ∇f.
9. Run GGVF on the improved vector field.
10. Run the snake on the final vector field until convergence.
11. Interpolate the snake to the next resolution level.
12. Set the image to the next resolution level.
13. Go to 3 until the highest resolution level is achieved.

The smoothing procedure employs the so-called quantile filter [53], which replaces all elements in the sampling window by the minimal (in this window) gray level. This step is problem specific. A variety of quantile and convolution filters can be utilized.

Note that steps 3–8 can be also applied as a part of the GGVF algorithm (inside the GGVF loop), creating a new ∇f at each step of GGVF. However, this entails a substantial increase in the computational time. Our experiments show that using steps 3–8 as a preprocessing step (preceding but not inside GGVF) at each level of MRA leads to good segmentation results. The algorithm can be applied with or without MRA, however, MRA often contributes considerably to the accuracy.

The gray level is increased by $f_{new} = \alpha f_{old}$, where α is a prescribed coefficient. If $f_{new} > 255$ at some points, the entire image is re-scaled. The coefficient is problem-depended. In our experiments we consider $\alpha = 1.5$.

Finally, it is often the case that the PPA combined with GGVF and applied to the lower resolution image produces an acceptable solution right away, so that the resulting snake is close enough to the true boundary. In this case the remaining steps require only GGVF to correct the active contour for the higher resolution images.

5. Numerical Experiments on Synthetic Images

The introductory numerical experiments have been conducted with synthetic images similar to those appearing in the ultrasonic imagery of the breast cancer (see Figs. 4 and 5). However, the synthetic images have simpler shapes, better contrast and are subjected to manually created single point noise and a brush-stroke noise.

Example 1. A simple synthetic image

Example 1 introduces a synthetic image with an additional impulse noise shown in Fig. 4. This time the GGVF-PPA is combined with multiresolution analysis (MRA) and compared with GGVF, GGVF-MRA and GGVF-MRA combined with the Gaussian smoothing (GS). The Gaussian smoothing applies to every multiresolution level. The parameters of the algorithms are problem-depended. They are hand-tuned and the methods are compared when they perform the best. (see a similar evaluation of the GVF based methods in [54]). The results are shown in Tables 2 and 3. Each cell in Table 2 and in all the forthcoming tables includes the following estimates. 1) The percentage of the true positives. 2) The average Hausdorff distance between true contour C_T and snake C_S given by

$$\mathrm{dist}_H(C_T, C_S)$$

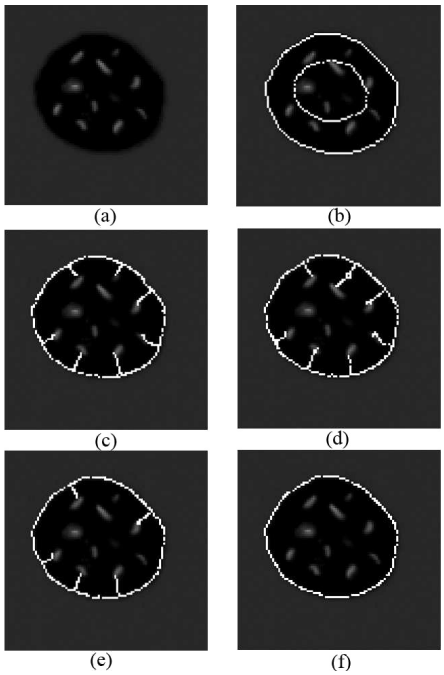

Fig. 4 Example 1. Simple synthetic image, (487 × 488 pixels). (a) The original image, (b) the initial contour and the ground truth, (c) GGVF, (d) GGVF-MRA, (e) GGVF-MRA-GS, (f) GGVF-MRA-PPA.

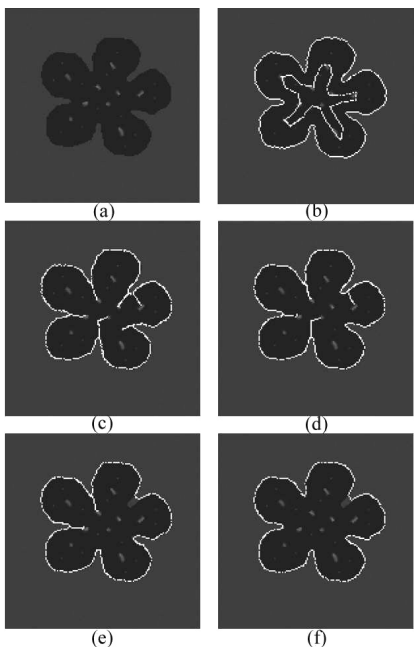

Fig. 5 Example 2. Synthetic image (593 × 593) with deep concavity. (a) The original image, (b) the initial contour and the ground truth, (c) GGVF, (d) GGVF-MRA, (e) GGVF-MRA-GS, (f) GGVF-MRA-PPA.

Table 2 Example 1. Accuracy (percentage of true positives and the Hausdorff distance) of GGVF, GGVF-MRA, GGVF-MRA-GS, and GGVF-MRA-PPA, (d = 4.7 pixels).

IT	GGVF		GGVF-MRA		GGVF-MRA-GS		GGVF-MRA-PPA	
	K		*K*		*K*		*K*	
	0.01	0.1	0.01	0.1	0.01	0.1	0.01	0.1
10	**71.053**	69.893	**72.254**	65.435	**69.806**	75.466	92.857	**100.00**
	1.421	1.465	**1.353**	1.686	**1.637**	1.206	0.736	**0.658**
	8.214	8.468	**7.822**	9.745	**9.462**	6.973	4.252	**3.804**
20	71.023	70.890	71.830	65.374	69.496	76.000	**94.118**	100.00
	1.390	1.465	1.402	1.795	1.595	1.270	**0.736**	0.663
	8.034	8.470	8.101	10.378	9.222	7.341	**4.252**	3.833
30	71.023	71.751	71.023	**65.790**	68.649	75.380	92.829	100.00
	1.391	1.409	1.358	**1.751**	1.684	1.237	0.736	0.662
	8.042	8.147	7.849	**10.121**	9.731	7.150	4.252	3.827
40	70.278	73.077	71.633	65.013	69.149	75.915	93.651	100.00
	1.411	1.392	1.364	1.748	1.703	1.239	0.736	0.665
	8.155	8.044	7.882	10.102	9.844	7.163	4.252	3.846
50	70.487	**73.950**	71.307	64.156	67.639	**76.220**	92.250	100.00
	1.404	**1.371**	1.351	1.732	1.704	**1.229**	0.736	0.665
	8.117	**7.926**	7.812	10.010	9.851	**7.106**	4.252	3.846

Table 3 Example 1. The best accuracy vs. the distance between the initial contour and the true boundary. (K = 0.01, K = 0.1, 50 iterations)

d (pixels)	GGVF		GGVF-MRA		GGVF-MRA-GS		GGVF-MRA-PPA	
	K		*K*		*K*		*K*	
	0.01	0.1	0.01	0.1	0.01	0.1	0.01	0.1
4.7	71.053	73.950	72.257	65.790	69.806	76.220	94.118	100.00
	1.421	1.371	1.353	1.751	1.637	1.229	0.736	0.658
	8.214	7.926	7.822	10.121	9.8462	7.106	4.252	3.804
6.8	45.694	51.724	55.309	54.122	49.072	52.857	85.024	97.059
	2.227	2.156	1.493	2.574	2.319	2.278	0.926	0.714
	16.243	14.012	12.971	13.561	14.284	13.855	5.102	4.239
8.4	20.786	27.670	32.685	30.256	32.801	40.541	68.019	77.483
	4.808	4.211	3.599	3.980	3.613	3.427	1.602	1.198
	22.977	20.349	20.023	22.784	19.970	18.001	9.973	6.725

$$= \frac{\sum\limits_{a\in C_T} \min\limits_{b\in C_S} \frac{\|a-b\|}{N_T} + \sum\limits_{a\in C_S} \min\limits_{b\in C_T} \frac{\|a-b\|}{N_S}}{2}, \tag{8}$$

where N_T and N_S is the number of points belonging to the true contour and the snake respectively.

3) A normalized average Hausdorff distance given by

$$\mathrm{dist}_{H,n}(C_T, C_S) = \frac{\mathrm{dist}_H(C_T, C_S)}{L_T} 10^3, \tag{9}$$

where L_T is the length of the true contour and 10^3 is the normalizing constant.

IT in Table 2 denotes the number of iterations. A bold font indicates the best result in the column.

The results in Table 3 show the best accuracy from 50 GVF iterations performed for K = 0.01 and K = 0.1.

Note that the Hausdorff distance divided by the length of the true contour L_T shows the relative importance of the error. For instance, the difference in 10 pixels is significant if the perimeter of the object is 100 pixels (a small object) but might not be that important if the length is 10000 pixels (a large object).

Furthermore, the advantage of Eq. (8)-Eq. (9) is that it is a distance in a mathematical sense, whereas, the number of true positives is not. A combination of the true positives and the Hausdorff distance Eq. (8)-Eq. (9) is a good measure of the segmentation quality. A larger degree of overlap of the boundaries (true positives) signifies a better segmentation. On the other hand, if the number of true positives is equal to zero, the boundaries could still be close, say at the distance of one pixel. In that case the Hausdorff distance shows that the quality of segmentation is still relatively good.

In turn, a set of boundaries dissimilar only over small portions may have the same Hausdorff distance as that of the globally dissimilar set of boundaries. However, if the boundaries are globally dissimilar we may expect a very low number of true positives. Finally, if the number of true positives is high and the Hausdorff distance is low, the quality of segmentation is very likely to be good.

The distance between the initial contour and the ground truth contour $d = \mathrm{dist}_H(C_T, C_{S,initial})$, where $C_{S,initial}$ is the initial snake. Clearly, the shape of the initial contour may effect the result as well. However, it is not the shape itself but the position of the strong noise relative to the initial contour. If the noise is still outside the contour, it may attract the snake and slow down the iterations or even decrease the accuracy. However, initializing the snake as a circle in the center of gravity of the tumor is a practical assumption.

The proposed method consistently outperforms the conventional techniques when the contour is initialized far

Table 4 Example 2. Accuracy: GGVF, GGVF-MRA, GGVF-MRA-GS, and GGVF-MRA-PPA, (d = 5.5).

IT	GGVF		GGVF-MRA		GGVF-MRA-GS		GGVF-MRA-PPA	
	K		*K*		*K*		*K*	
	0.01	0.1	0.01	0.1	0.01	0.1	0.01	0.1
10	73.568	74.322	83.133	85.641	87.928	85.500	93.241	99.772
	1.642	1.571	1.356	1.314	1.226	1.454	1.000	0.910
	4.147	3.967	3.423	3.319	3.095	3.672	2.526	2.297
20	73.058	78.915	82.993	**86.395**	87.616	92.927	92.969	99.771
	1.603	1.489	1.403	**1.317**	1.264	1.083	1.006	0.888
	4.048	3.759	3.542	**3.327**	3.191	2.736	2.540	2.242
30	73.104	79.284	82.706	85.378	**88.869**	93.200	93.137	99.770
	1.605	1.446	1.394	1.298	**1.280**	1.100	1.004	0.889
	4.052	3.651	3.521	3.219	**3.232**	2.778	2.537	2.244
40	**74.111**	81.037	**83.646**	81.487	88.321	**93.294**	92.927	99.767
	1.604	1.445	**1.439**	1.302	1.270	**1.109**	1.004	0.890
	4.050	3.649	**3.633**	3.288	3.208	**2.800**	2.536	2.248
50	72.558	**81.745**	82.586	81.013	88.246	93.097	**93.439**	**99.774**
	1.568	**1.441**	1.411	1.307	1.234	1.095	**1.004**	**0.891**
	3.959	**3.638**	3.562	3.300	3.115	2.764	**2.537**	**2.249**

Table 5 Example 2. The best accuracy vs. the distance between the initial contour and the true boundary. (K = 0.01, K = 0.1, 50 iterations)

d (pixels)	GGVF		GGVF-MRA		GGVF-MRA-GS		GGVF-MRA-PPA	
	K		*K*		*K*		*K*	
	0.01	0.1	0.01	0.1	0.01	0.1	0.01	0.1
5.5	74.111	81.745	83.646	86.395	88.869	93.294	93.439	99.774
	1.604	1.489	1.439	1.317	1.280	1.083	1.004	0.891
	4.050	3.759	3.633	3.327	3.232	2.736	2.537	1.249
7.4	42.521	57.760	56.636	60.694	60.238	69.614	85.631	88.972
	4.262	2.883	2.941	2.739	2.799	1.876	1.406	1.291
	11.059	7.280	7.122	6.917	6.989	4.736	3.428	3.259
8.8	30.922	46.939	50.826	59.100	53.333	61.868	74.497	82.843
	5.909	4.624	4.423	3.703	3.880	2.444	2.009	1.776
	13.446	11.675	10.825	9.351	9.864	6.171	5.453	4.484

from the boundary of the object (Tables 2 and 3). It is possible to achieve the 100 percent accuracy when the contour is initialized close to the boundary (see our forthcoming numerical examples and tables of the accuracy vs. the distance between the snake and the actual contour). For this experiment, number of multiresolution levels $N_L = 2$, $\Delta_1 = 0.7$, $\Delta_2 = 0.2$ and the window size $S_{max} = 4 \times 4$.

Example 2. A synthetic image with deep concavity

The results above are supported by Example 2. The synthetic image with deep concavities distorted by the noise is displayed in Fig. 5. The accuracy and sensitivity shown in Tables 4 and 5 make it possible to conjecture that the proposed techniques could be performing equally efficient on real ultrasound images. For this experiment, $N_L = 2$, $\Delta_1 = 0.7$, $\Delta_2 = 0.2$ and $S_{max} = 4 \times 4$.

6. Numerical Experiments with Ultrasound Images of Breast Tumors

Detection of tumors in the ultrasound (US) images by a trained physician is usually efficient and the number of false negatives is low. However, manual segmentation of the tumor boundary is tedious and time-consuming. Therefore,

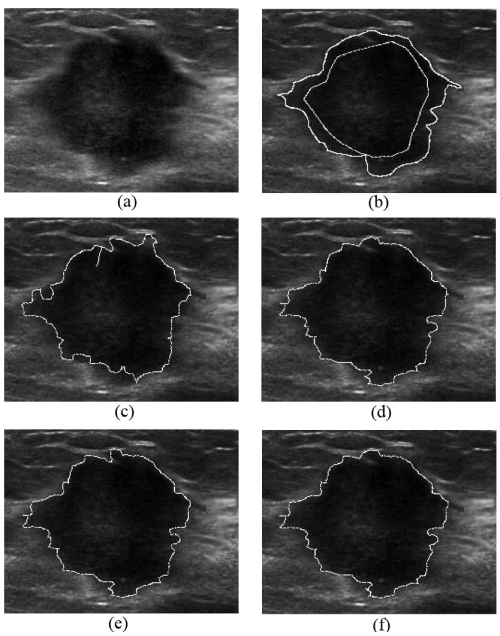

Fig. 6 Example 3. Low contrast US image, (782×616), (d = 11) (a) The original image, (b) the initial contour and the ground truth, (c) GGVF, (d) GGVF-MRA, (e) GGVF-MRA-GS, (f) GGVF-MRA-PPA.

Table 6 Example 3. Accuracy: GGVF, GGVF-MRA, GGVF-MRA-GS, and GGVF-MRA-PPA, (d = 11).

IT	GGVF		GGVF-MRA		GGVF-MRA-GS		GGVF-MRA-PPA	
	K		*K*		*K*		*K*	
	0.01	0.1	0.01	0.1	0.01	0.1	0.01	0.1
10	28.723	50.000	74.136	89.568	90.188	85.886	**90.476**	89.374
	7.781	5.483	3.799	1.673	1.636	1.738	**1.545**	1.467
	10.347	7.292	5.052	2.225	2.841	2.311	**2.252**	1.951
20	27.721	53.555	73.212	**90.530**	89.403	86.342	90.293	88.872
	7.955	5.103	3.821	**1.624**	1.638	1.758	1.453	1.464
	10.578	6.786	5.082	**2.160**	2.843	2.338	3.263	1.947
30	27.762	54.096	75.107	89.921	89.580	**86.903**	89.676	**89.732**
	7.961	4.961	3.818	1.645	1.642	**1.737**	1.443	**1.494**
	10.586	6.598	5.077	2.187	2.848	**2.310**	2.249	**1.986**
40	28.781	54.138	**75.648**	89.314	90.332	86.793	89.580	85.242
	7.942	4.488	**3.820**	1.627	1.542	1.785	1.404	1.501
	10.562	5.968	**5.079**	2.164	2.828	2.373	3.196	1.996
50	**29.293**	**59.085**	73.625	84.849	**90.688**	81.409	89.580	89.686
	7.873	**3.755**	3.816	1.654	**1.142**	1.779	1.403	1.403
	10.469	**4.994**	5.075	2.200	**2.848**	2.366	3.195	1.999

Table 7 Example 3. Accuracy: GGVF, GGVF-MRA, GGVF-MRA-GS, and GGVF-MRA-PPA, (d = 17).

IT	GGVF		GGVF-MRA		GGVF-MRA-GS		GGVF-MRA-PPA	
	K		*K*		*K*		*K*	
	0.01	0.1	0.01	0.1	0.01	0.1	0.01	0.1
10	14.439	29.692	**55.177**	89.587	62.319	86.283	89.466	**90.075**
	13.931	10.675	**5.928**	1.670	5.701	1.794	1.643	**1.641**
	18.525	14.196	**7.883**	2.122	7.581	2.522	2.137	**1.943**
20	14.985	28.656	51.948	89.711	62.179	**87.132**	**89.808**	89.561
	13.747	10.205	6.168	1.631	5.730	**1.742**	**1.680**	1.442
	18.280	13.570	8.202	2.169	7.619	**2.316**	**2.235**	1.918
30	16.539	35.356	50.743	**89.715**	61.057	86.758	89.105	89.259
	12.267	8.638	6.889	**1.657**	5.427	1.732	1.767	1.448
	16.312	11.487	9.160	**2.204**	7.217	2.303	2.349	1.925
40	18.386	38.570	49.449	89.465	61.388	86.636	89.313	89.614
	11.645	7.140	6.979	1.695	5.908	1.937	1.728	1.500
	15.485	9.495	9.281	2.254	7.857	2.313	2.297	1.995
50	**20.027**	**42.154**	51.386	80.355	**64.151**	78.415	89.313	89.971
	11.585	**6.975**	6.649	2.641	**5.371**	1.716	1.741	1.670
	15.406	**9.275**	8.841	3.183	**7.142**	3.282	2.315	2.217

automatic segmentation techniques are important to help us to better visualize the tumor boundary, to calculate the volume of the tumor and to extract features needed for the tumor classification (benign or malignant).

Example 3. A low contrast malignant tumor

The example of a tumor shown in Fig. 6 shows convergence of GGVF combined with different noise removal methods for varying diffusion coefficients (6). The snake has been initialized at an average Hausdorff distance of approximately 11, 17 and 22 pixels from the true boundary as follows. First, the snake is initialized inside a binary ground truth image which is "black" inside the tumor and "white" outside. Next, we let the snake grow until it reaches a certain distance from the boundary. Finally, we use this contour as the initial snake inside the real ultrasound image. Convergence of the GGVF iterations is analyzed for extreme values of the diffusion coefficients: $K = 0.01$ (slow diffusion) and $K = 0.1$ (relatively high diffusion). The ground truth contours were outlined by Dr. Mavin Wongsaisuvan, who is currently a leading radiologist with the Queen Sirikit Center for Breast Cancer of King Chulalongkorn Memorial Hospital, Bangkok Thailand. Tables 6, 7 and 8 and Figs. 6, 7 and 8 demonstrate that when the snake is initialized close to the boundary, GGVF-MRA-GS and GGVF-MRA-PPA perform equally well. However, when the contour is initialized far from the boundary, GGVF-MRA-PPA outperforms GGVF-MRA-GS, GGVF-MRA and the conventional GGVF. For example, when the contour is initialized at 22 pixels from the true boundary, the best result produced GGVF-MRA-PPA for $K = 0.1$ is by 20 percent better than GGVF-MRA-GS in terms of the true positive points. In turn, the Hausdroff distance is 5 times (!) smaller (Table 8). This is because the contours are different along a significant part of the boundary shown in Fig. 8. The best results produced by the methods being compared versus the distance from the true boundary are given in Table 9. For this experiment, $N_L = 3$, $\Delta_1 = 0.81$, $\Delta_2 = 0.1$ and $S_{max} = 15 \times 15$.

Table 8 Example 3. Accuracy: GGVF, GGVF-MRA, GGVF-MRA-GS, and GGVF-MRA-PPA, (d = 22).

IT	GGVF		GGVF-MRA		GGVF-MRA-GS		GGVF-MRA-PPA	
	K		*K*		*K*		*K*	
	0.01	0.1	0.01	0.1	0.01	0.1	0.01	0.1
10	10.421	12.406	41.879	68.374	**59.660**	63.390	90.961	90.569
	22.168	19.724	12.526	8.712	**12.199**	9.839	2.002	1.475
	29.478	26.229	16.656	11.585	**16.222**	12.485	2.662	1.962
20	16.634	28.898	40.479	68.895	57.188	68.759	90.585	**90.986**
	19.029	17.652	12.632	8.811	12.188	6.941	2.278	**1.441**
	25.305	23.473	16.798	11.717	16.208	9.230	3.029	**1.916**
30	16.581	29.851	42.760	71.329	59.499	**71.965**	90.490	89.790
	19.066	18.357	12.336	8.626	12.162	**6.600**	1.671	1.457
	25.354	24.411	16.405	11.470	16.173	**8.777**	2.222	1.938
40	14.726	27.504	**43.247**	67.194	58.578	67.376	**91.396**	90.638
	19.393	18.091	**12.432**	8.935	12.031	7.114	**1.690**	1.483
	25.789	24.057	**16.532**	11.881	15.999	9.460	**2.247**	1.972
50	**16.526**	**29.930**	42.645	**72.873**	58.372	69.154	91.396	90.371
	19.224	**18.289**	12.437	**8.237**	12.112	7.091	1.700	1.758
	25.564	**24.230**	16.539	**10.953**	16.107	9.430	2.261	2.338

Table 9 Example 3. The best accuracy vs. the distance between the initial contour and the true boundary (K = 0.01, K = 0.1, 50 iterations).

d (pixels)	GGVF		GGVF-MRA		GGVF-MRA-GS		GGVF-MRA-PPA	
	K		*K*		*K*		*K*	
	0.01	0.1	0.01	0.1	0.01	0.1	0.01	0.1
11.0	29.293	59.085	75.648	90.530	90.688	86.903	90.476	89.732
	7.873	3.755	3.820	1.624	1.142	1.737	1.545	1.494
	10.469	4.994	5.079	2.160	2.848	2.310	2.252	1.986
17.4	20.027	42.154	55.177	89.715	64.151	87.132	89.808	90.075
	11.585	6.975	5.928	1.657	5.371	1.742	1.680	1.641
	15.406	9.275	7.883	2.204	7.142	2.316	2.235	1.943
21.9	16.526	29.930	43.247	72.873	59.660	71.965	91.396	90.986
	19.224	18.289	12.432	8.237	12.199	6.600	1.690	1.441
	25.564	24.230	16.532	10.953	16.222	8.777	2.247	1.916

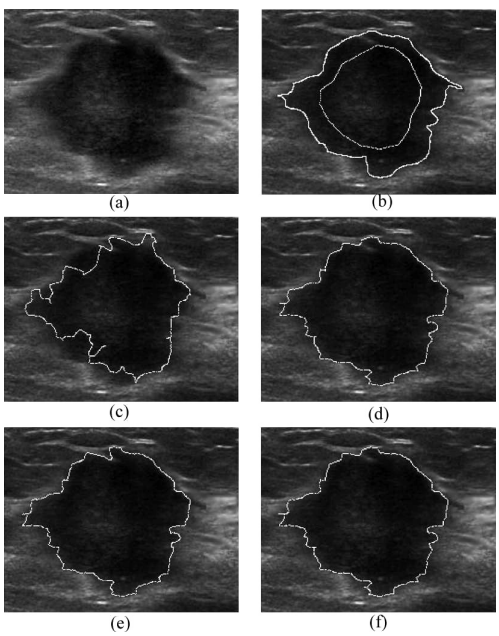

Fig. 7 Example 3. Low contrast US image, (d = 17) (a) The original image, (b) the initial contour and the ground truth, (c) GGVF, (d) GGVF-MRA, (e) GGVF-MRA-GS, (f) GGVF-MRA-PPA.

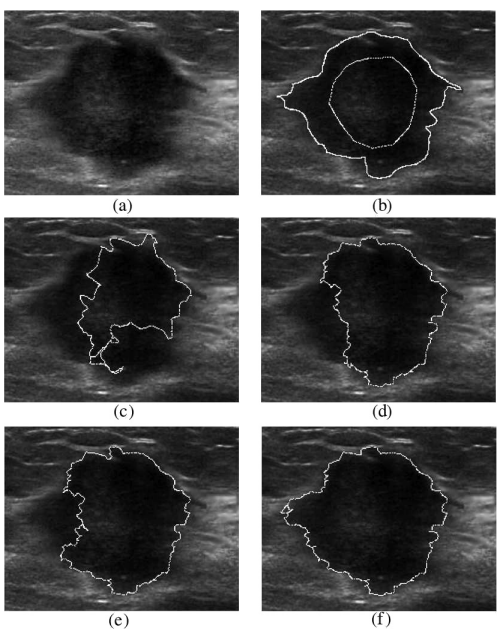

Fig. 8 Example 3. Low contrast US image, (d = 22) (a) The original image, (b) the initial contour and the ground truth, (c) GGVF, (d) GGVF-MRA, (e) GGVF-MRA-GS, (f) GGVF-MRA-PPA.

Example 4. A low contrast malignant tumor. Complicated shape. High noise

As opposed to Example 3 the structure of the noise is much more complicated. The image from Example 3 is characterized by an almost uniform background inside the tumor and a single large group of noise (see the two images scaled to 0–255 in Fig. 9). This noise can be detected in one pass when the sampling window becomes large enough. As opposed to that the noise in Example 4 is scattered across the entire tumor. The noise includes several clusters some of which are very close to the true boundary. Clearly, such noise structures are hard to classify and eliminate.

The low contrast and very complicated, "fuzzy" boundary make segmentation of the tumor in Fig. 10 untractable for conventional GGVF (Fig. 10 (c)). However, GGVF enhanced by MRA and a smoother works much better. Figures 10, 11 and Tables 10 compare the performance of the proposed method with GGVF-MRA and GGVF-MRA-GS. The procedures display a close accuracy when the snake is initialized at $d = 9.1$ from the boundary. Furthermore, for $d = 12.6$ the proposed method is slightly better if $K = 0.1$. However, it strongly outperforms other methods for $K = 0.01$ (see Table 10 and Fig. 11 (c)–(f)). This could be explained by smoothing effects of GGVF for large K. Nevertheless, large K is not always possible because large diffusion often destroys the true boundary. It is much safer to run GGVF with small K and correct the noise by PPA. The local nature of PPA makes it possible to smooth only noisy area

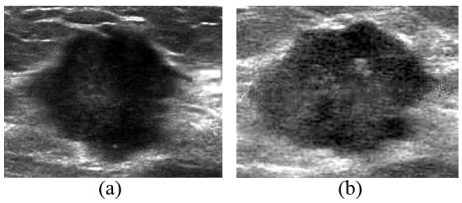

Fig. 9 Scaled images from (a) Example 3, (b) Example 4.

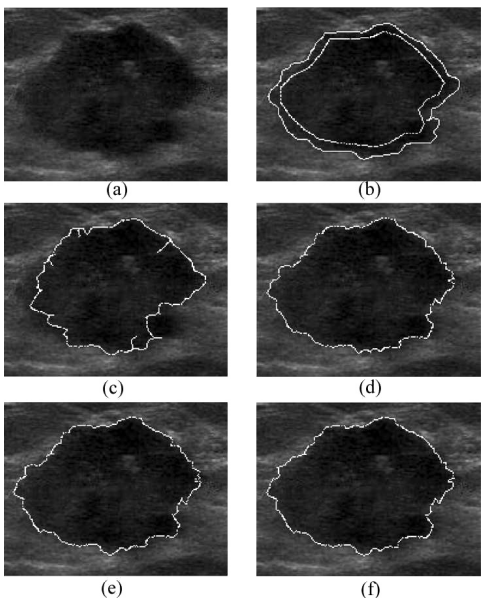

Fig. 10 Example 4. Low contrast US image (687 × 535), ($d = 9.1$) (a) The original image, (b) the initial contour and the ground truth, (c) GGVF, (d) GGVF-MRA, (e) GGVF-MRA-GS, (f) GGVF-MRA-PPA.

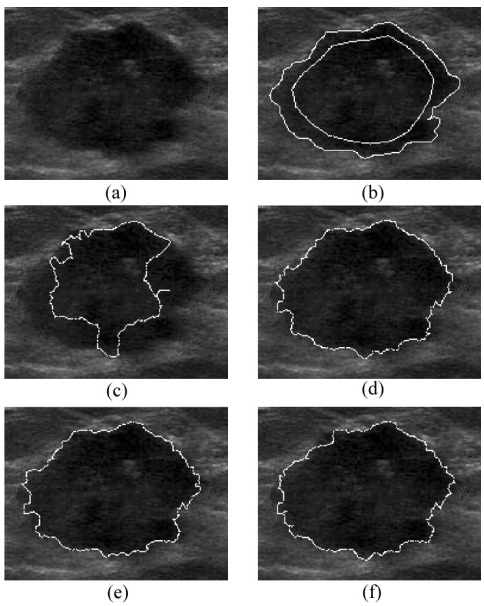

Fig. 11 Example 4. Low contrast US image, ($d = 12.6$) (a) The original image, (b) the initial contour and the ground truth, (c) GGVF, (d) GGVF-MRA, (e) GGVF-MRA-GS, (f) GGVF-MRA-PPA.

Table 10 Example 4. The best accuracy vs. the distance between the initial contour and the true boundary ($K = 0.01$, $K = 0.1$, 50 iterations).

d (pixels)	GGVF		GGVF-MRA		GGVF-MRA-GS		GGVF-MRA-PPA	
	K		K		K		K	
	0.01	0.1	0.01	0.1	0.01	0.1	0.01	0.1
6.8	59.678	65.605	79.266	85.259	82.154	83.960	85.003	85.230
	3.807	3.200	2.563	1.791	2.199	1.903	1.809	1.781
	15.042	10.988	5.121	3.459	4.028	3.506	3.615	2.978
9.1	26.032	56.899	67.325	83.534	82.004	83.951	86.465	86.627
	9.058	3.998	3.146	1.956	2.144	2.012	1.741	1.690
	14.446	9.103	6.218	3.468	3.891	3.517	2.448	2.370
12.6	12.185	22.179	26.460	75.960	36.137	77.688	68.379	80.738
	18.057	11.672	8.703	2.923	7.096	2.681	3.095	2.427
	30.258	27.159	25.406	4.505	21.058	4.306	11.706	3.125

while enhancing the boundary regions. For this experiment, $N_L = 3$, $\Delta_1 = 0.85$, $\Delta_2 = 0.1$ and $S_{max} = 10 \times 10$.

Example 5. Low contrast tumor subjected to a Gaussian and a "salt and pepper" noise as follows:

Consider a round benign tumor depicted in Fig. 12. Since the tumor has a relatively simple shape, the conventional GGVF, GGVF-MRA, GGVF-MRA-GS and GGVF-MRA-PPA work equally well. An accuracy above 90% is achieved by each method for large K in Table 11. The image contains a noise induced by the US device and the irregularities of the human tissues. On the top of this "natural" noise we subject the image to the Gaussian and salt and paper noise with varying intensity. The Gaussian noise is applied with the zero mean and 0.02 variance. The effect of the Gaussian noise is then measured in terms of the signal-to-noise Ratio (SNR). Table 12 shows that the performance of the proposed method applied to suppress the Gaussian noise is still comparable with GGVF, GGVF-MRA, GGVF-MRA-GS. In other words PPA does not display significant

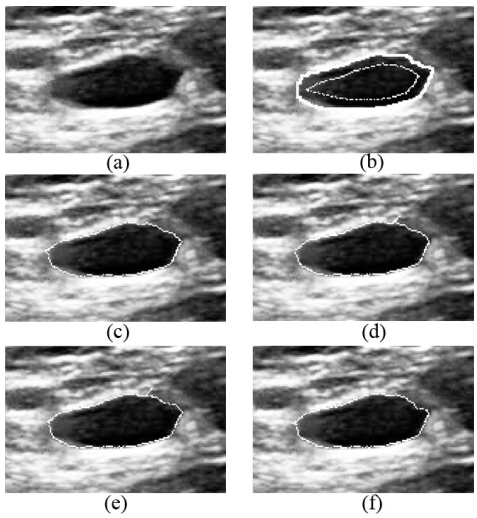

Fig. 12 Example 5. Low contrast US image, (625×415) (a) The original image, (b) the initial contour and the ground truth, (c) GGVF, (d) GGVF-MRA, (e) GGVF-MRA-GS, (f) GGVF-MRA-PPA.

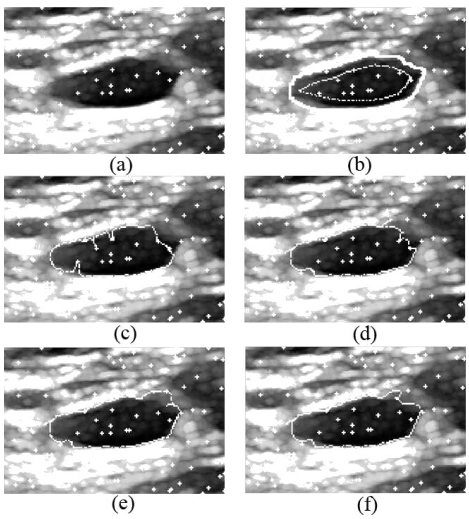

Fig. 13 Example 5. Low contrast US image. Salt and pepper noise with the intensity $n_d = 1\%$ ($SNR = 25\,dB$). (a) The original image, (b) the initial contour and the ground truth, (c) GGVF, (d) GGVF-MRA, (e) GGVF-MRA-GS, (f) GGVF-MRA-PPA.

Table 11 Example 5. The best accuracy for the original image: GGVF, GGVF-MRA, GGVF-MRA-GS, and GGVF-MRA-PPA (50 iterations).

	GGVF		GGVF-MRA		GGVF-MRA-GS		GGVF-MRA-PPA	
	K		K		K		K	
	0.01	0.1	0.01	0.1	0.01	0.1	0.01	0.1
Best	40.694	93.905	81.356	97.287	83.280	97.701	86.923	97.600
	4.764	2.475	1.856	0.917	1.493	0.905	1.137	0.978
	9.448	5.027	4.359	2.369	3.306	1.145	2.496	1.211

Table 12 The best accuracy vs. the SNR. ($K = 0.1$, 50 iterations)

$SNR(dB)$	GGVF	GGVF-MRA	GGVF-MRA-GS	GGVF-MRA-PPA
Non-noised	42.154	89.189	88.551	93.425
	6.975	1.641	1.716	1.589
	9.275	2.183	2.282	2.113
30	37.630	90.504	89.630	93.053
	8.680	1.595	1.661	1.523
	11.543	2.121	2.209	2.012
25	41.718	90.882	87.161	93.125
	7.465	1.531	1.647	1.490
	9.927	2.036	2.191	1.993
20	33.195	88.842	86.883	91.499
	9.102	1.624	1.726	1.490
	12.104	2.160	2.295	1.982
15	25.337	84.569	83.578	86.896
	11.791	1.771	1.834	1.702
	15.679	2.355	2.438	2.263

Table 13 Example 5. The best accuracy for the Salt and Pepper noise image, $n_d = 1\%$ ($SNR = 25\,dB$): GGVF, GGVF-MRA, GGVF-MRA-GS, and GGVF-MRA-PPA (50 iterations).

	GGVF		GGVF-MRA		GGVF-MRA-GS		GGVF-MRA-PPA	
	K		K		K		K	
	0.01	0.1	0.01	0.1	0.01	0.1	0.01	0.1
Best	39.465	75.410	68.687	90.164	87.391	93.976	97.917	96.761
	5.401	3.839	3.615	1.804	2.231	1.475	1.054	1.196
	9.982	7.149	7.302	3.490	4.478	3.206	2.241	2.303

Table 14 Example 5. The best accuracy for the Salt and Pepper noise image, $n_d = 3\%$ ($SNR = 20\,dB$): GGVF, GGVF-MRA, GGVF-MRA-GS, and GGVF-MRA-PPA (50 iterations).

	GGVF		GGVF-MRA		GGVF-MRA-GS		GGVF-MRA-PPA	
	K		K		K		K	
	0.01	0.1	0.01	0.1	0.01	0.1	0.01	0.1
Best	27.985	46.939	61.603	84.791	89.627	89.290	95.175	97.083
	5.882	5.331	3.777	2.005	1.843	1.944	1.182	0.975
	11.459	9.758	7.230	4.480	4.138	4.297	2.833	2.567

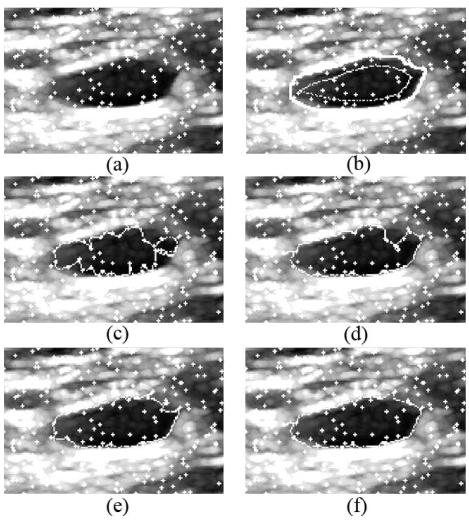

Fig. 14 Example 5. Low contrast US image. Salt and pepper noise, $n_d = 3\%$ ($SNR = 20\,dB$). (a) The original image, (b) the initial contour and the ground truth, (c) GGVF, (d) GGVF-MRA, (e) GGVF-MRA-GS, (f) GGVF-MRA-PPA.

benefits. However, the method works much better as applied to images subjected to the dilated salt and paper noise. The salt and pepper noise is applied with the percentage of corrupted pixels $n_d = 1\%$ and $n_d = 3\%$. The corrupted pixels are set randomly to 255 or 0. Additionally, the pixels with the values 255 (salt) are dilated by one pixel to create false boundaries. The black pixels (pepper) are not dilated. The background of the tumor is usually dark, therefore, the pepper noise will not create false boundaries. (see Fig. 13 and 14). Table 13 shows the accuracy increase in terms of true positives of about 10% for the low diffusion and 3% for the high diffusion. The increase in terms of the Hausdorff distance for low diffusion is about 2 times compared to GGVF-MRA-GS. Table 14 displays the effects of a higher intensity salt and pepper noise. It shows the accuracy increase in terms of true positives of about 6%. However, the Hausdorff error improvement is still very impressive about 2 times for the low and the high diffusion depending on K. For this experiment, $N_L = 2$, $\Delta_1 = 0.5$, $\Delta_2 = 0.15$ and $S_{max} = 3 \times 3$.

7. Conclusions

The proposed combination of the phase portrait analysis and multiresolution filter bank generalizes preceding discrete force field analysis routines designed for generalized gradient vector flow method. The method applied to the US tumor images of breast is capable of increasing the accuracy of the segmentation up to 10 times in terms of the normalized Hausdorff distance and up to 20% in terms of true positives.

The method shows clear benefits when applied to the initial contour positioned far from the true boundary. Due to its local nature, the method works very well with the noise represented by large group of pixels with the intensity different from the local background such as the salt and pepper noise.

The numerical experiments make it possible to conjecture that the proposed techniques will succeed in segmentation of a variety of tumors displayed in ultrasound images of the breast.

Acknowledgement

We thank Dr. Mawin Wongsaisuvan with the Queen Sirikit Center for Breast Cancer of King Chulalongkorn Memorial Hospital for providing the ground truth contours and useful comments.

We wish to thank the anonymous referees of this paper for very useful comments and attention to details.

This research is sponsored by Thailand Research Fund grant BRG 5380016.

References

[1] M. Kass, A. Witkin, and D. Terzopoulos, "Snakes: Active contour models," Int. J. Comput. Vis., vol.1, no.4, pp.321–331, 1988.

[2] D. Kuan, A. Sawdhuck, T. Strand, and P. Chavel, "Adaptive restoration of image with speckle," IEEE Trans. Acoust. Speech Signal Process., vol.ASSP-35, no.3, pp.373–383, 1987.
[3] A. Evans and M. Nixon, "Biased motion-adaptive temporal filtering for speckle reduction in echocardiography," IEEE Trans. Med. Imaging, vol.15, no.1, pp.39–50, 1996.
[4] F. Lefebvre, G. Berger, and P. Laugier, "Automatic detection of the boundary of the calcaneus from ultrasound parametric images using an active contour model: Clinical assessment," IEEE Trans. Med. Imaging, vol.17, no.1, pp.45–52, 1998.
[5] Y.S. Akgul, C. Kambhamettu, and M. Stone, "Extraction and tracking of the tongue surface from ultrasound image sequences," Proc. IEEE Computer Society Conference on Computer Vision and Pattern Recognition (CVPR '98), pp.298–303, IEEE Computer Society, 1998.
[6] R. Chung and K.K. Ho, "Using 2D active contour models for 3D reconstruction from serial sections," International Conference on Pattern Recognition, vol.1, pp.849–853, 1996.
[7] A. Fenster, S. Tong, H. Cardinal, C. Blake, and D. Downey, "Three-dimensional ultrasound imaging system for prostate cancer diagnosis and treatment," IEEE Trans. Instrum. Meas., vol.47, no.6, pp.1439–1447, 1998.
[8] M. Strintzis and I. Kokkinidis, "Maximum likelihood motion estimation in ultrasound image sequences," IEEE Signal Process. Lett., vol.4, no.6, pp.156–157, 1997.
[9] D. Chen, R. Chang, W. Wu, W. Moon, and W. Wu, "3-D breast ultrasound segmentation using active contour model," Ultrasound in Medicine and Biology, vol.29, no.7, pp.1017–1026, 2003.
[10] R. Chang, W. Wu, W. Moon, W. Lee, and D. Chen, "Segmentation of breast tumor in three-dimensional ultrasound images using three-dimensional discrete active contour model," Ultrasound in Medicine and Biology, vol.29, no.11, pp.1571–1581, 2003.
[11] M. Cvancarova, F. Albresgtsen, K. Brabrand, and E. Samset, "Segmentation of ultrasound images of liver tumors applying snake algorithms and gvf," Congress Series, vol.1281, pp.218–223, 2005.
[12] M. Aleman-Flores, P. Aleman-Flores, L. Alvarez-Leon, M. Esteban-Sanchez, R. Fuentes-Pavon, and J. Santana-Montesdeoca, "Computerized ultrasound characterization of breast tumors," International Congress Series, vol.1281, pp.1063–1068, 2005.
[13] L.D. Cohen, "On active contour models and balloons," Comput. Vis. Graph. Image Process., Image Understanding, vol.53, no.2, pp.211–218, 1991.
[14] L.D. Cohen and I. Cohen, "Finite element methods for active contour models and balloons for 2D and 3D images," IEEE Trans. Pattern Anal. Mach. Intell., vol.15, pp.1131–1147, 1991.
[15] T. Mcinerney and D. Terzopoulos, "T-snakes: Topology adaptive snakes," Medical Image Analysis, vol.4, pp.73–91, 2000.
[16] G. Giraldi, E. Strauss, and A. Oliveira, "Dual-t-snakes model for medical imaging segmentation," Pattern Recognit. Lett., vol.24, no.7, pp.993–1003, 2003.
[17] H. Delingette and J. Montagnat, "New algorithms for controlling active contours shape and topology," European Conference on Computer Vision (ECCV'2000), LNCS, no.1843, pp.381–395, Springer, 2000.
[18] H. Delingette and J. Montagnat, "Shape and topology constraints on parametric active contours," Computer Vision and Image Understanding, vol.83, pp.140–171, 2000.
[19] B. Olstad and A.H. Torp, "Encoding of a priori information in active contour models," IEEE Trans. Pattern Anal. Mach. Intell., vol.18, no.9, pp.863–872, 1996.
[20] S.D. Fenster and J.R. Kender, "Sectored snakes: Evaluating learned-energy segmentations," IEEE Trans. Pattern Anal. Mach. Intell., vol.23, no.9, pp.1028–1034, 2001.
[21] M.A. Charmi, S. Derrode, and F. Ghorbel, "Fourier-based geometric shape prior for snakes," Pattern Recognit. Lett., vol.29, no.7, pp.897–904, 2008.
[22] R. Ronfard, "Region based strategies for active contour models," Oct. 1994.
[23] A. Chakraborty, L. Staib, and J. Duncan, "Deformable boundary finding in medical images by integrating gradient and region information," IEEE Trans. Med. Imaging, vol.15, no.6, pp.859–870, 1996.
[24] S.C. Zhu and A. Yuille, "Region competition: Unifying snakes, region growing, and bayes/mdl for multiband image segmentation," IEEE Trans. Pattern Anal. Mach. Intell., vol.18, no.9, pp.884–900, 1996.
[25] R. Malladi, J.A. Sethian, and B.C. Vemuri, "Shape modeling with front propagation: A level set approach," IEEE Trans. Pattern Anal. Mach. Intell., vol.17, no.2, pp.158–175, Feb. 1995.
[26] S. Osher and J.A. Sethian, "Fronts propagating with curvature-dependent speed: Algorithms based on hamilton-Jacobi formulations," J. Computational Physics, vol.79, pp.12–49, 1988.
[27] V. Caselles, R. Kimmel, and G. Sapiro, "Geodesic active contours," Int. J. Comput. Vis., vol.22, no.1, pp.61–79, Feb. 1997.
[28] K. Siddiqi, Y.B. Lauzie're, A. Tannenbaum, and S.W. Zucker, "Area and length minimizing flows for shape segmentation," IEEE Trans. Image Process., vol.7, no.3, pp.433–443, 1998.
[29] X. Wang, L. He, and W.G. Wee, "Deformable contour method: A constrained optimization approach," Int. J. Comput. Vis., vol.59, no.1, pp.87–108, 2004.
[30] L. He, Z. Peng, B. Everding, X. Wang, C. Han, K. Weiss, and W. Wee, "A comparative study of deformable contour methods on medical image segmentation," Image Vis. Comput., vol.26, no.2, pp.141–163, Feb. 2008.
[31] A. Yezzi, S. Kichenassamy, A. Kumar, P. Olver, and A. Tannenbaum, "A geometric snake model for segmentation of medical imagery," IEEE Trans. Med. Imaging, pp.199–209, 1997.
[32] M. Rochery, I.H. Jermyn, and J. Zerubia, "Higher order active contours.," Int. J. Comput. Vis., vol.69, no.1, pp.27–42, 2006.
[33] J.M. Fitzpatrick and M. Sonka, Handbook of Medical Imaging, Volume 2. Medical Image Processing and Analysis (SPIE Press Monograph vol.PM80), 1st ed., SPIE–The International Society for Optical Engineering, June 2000.
[34] C. Li, J. Liu, and M.D. Fox, "Segmentation of external force field for automatic initialization and splitting of snakes," Pattern Recognit., vol.38, no.11, pp.1947–1960, 2005.
[35] C. Xu and J.L. Prince, "Snakes, shapes, and gradient vector flow," IEEE Trans. Image Process., vol.7, no.3, pp.359–369, 1998.
[36] C. Xu and J.L. Prince, "Gradient vector flow: A new external force for snakes," Proc. International IEEE Computer Society Conference on Computer Vision and Pattern Recognition, pp.66–71, 1997.
[37] C. Xu and J.L. Prince, "Generalized gradient vector flow external forces for active contours," Signal Process., vol.71, no.2, pp.131–139, 1998.
[38] J. Tang, "A multi-direction gvf snake for the segmentation of skin cancer images," Pattern Recognit., vol.42, no.6, pp.1172–1179, 2009.
[39] M. Wei, Y. Zhou, and M. Wan, "A fast snake model based on non-linear diffusion for medical image segmentation," Computerized Medical Imaging and Graphics, vol.28, no.3, 2004.
[40] Z. Hou and C. Han, "Force field analysis snake: An improved parametric active contour model," Pattern Recognit. Lett., vol.26, no.5, pp.513–526, 2005.
[41] C.F. Shu and R.C. Jain, "Vector field analysis for oriented patterns," IEEE Trans. Pattern Anal. Mach. Intell., vol.16, no.9, pp.946–950, 1994.
[42] W.Y. Yau, J. Li, and H. Wang, "Nonlinear phase portrait modeling of fingerprint orientation," Control, Automation, Robotics and Vision Conference, pp.1262–1267, 2004.
[43] J. Li, W.Y. Yau, and H. Wang, "Constrained nonlinear models of fingerprint orientations with prediction," Pattern Recognit., vol.39, no.1, pp.102–114, 2006.
[44] J. Li, W.Y. Yau, and H. Wang, "Combining singular points and orientation image information for fingerprint classification," Pattern

Recognit., vol.41, no.1, pp.353–366, 2008.
[45] X. Tian, S. Samarasinghe, and G. Murphy, "An integrated algorithm for detecting position and size of knots on logs using texture analysis," Proc. Conference on Image and Visions Computing, pp.121–132, 1999.
[46] I. Cohen and I. Herlin, "A motion computation and interpretation framework for oceanographic satellite images," Computer Vision, International Symposium on, pp.13–18, 1995.
[47] I. Cohen, I. Herlin, and I. Rocquencourt, "Optical flow and phase portrait methods for environmental satellite image sequences," Proc. 4th European Conference on Computer Vision-Volume II, pp.141–150, Springer-Verlag, 1996.
[48] R. Rangayyan and F. Ayres, "Gabor filters and phase portraits for the detection of architectural distortion in mammograms," Medical and Biological Engineering and Computing, vol.44, pp.883–894, 2006.
[49] D. Jordan and P. Smith, Nonlinear ordinary differential equations: An introduction for scientists and engineers / D.W. Jordan and P. Smith, 4th ed., Oxford University Press, Oxford, New York, 2007. Previous ed.: 1999.
[50] I. Daubechies, Ten Lectures on Wavelets, CBMS-NSF Reg. Conf. Series in Applied Math., SIAM, 1992.
[51] M. Mignotte and J. Meunier, "A multiscale optimization approach for the dynamic contour-based boundary detection issue," Computerized Medical Imaging and Graphics, vol.25, no.3, pp.265–275, 2001.
[52] N. Ray, B. Chanda, and J. Das, "A fast and flexible multiresolution snake with a definite termination criterion," Pattern Recognit., vol.34, no.7, pp.1483–1490, 2001.
[53] A. Bengtsson and H. Bengtsson, "Microarray image analysis: Background estimation using quantile and morphological filters," BMC Bioinformatics, vol.7, p.96, 2006.
[54] L. He, Z. Peng, B. Everding, X. Wang, C.Y. Han, K.L. Weiss, and W.G. Wee, "Review: A comparative study of deformable contour methods on medical image segmentation," Image Vis. Comput., vol.26, no.2, pp.141–163, 2008.

Sirikan Chucherd received the B.E. and M.E. degrees in electrical engineering from King Mongkut's Institute of Technology Ladkrabang of Thailand in 1998 and 2001 respectively. Currently she is a Ph.D. student in Information Technology at Sirindhorn International Institute of Technology, Thammasat University of Thailand. Her research interests include medical image processing and pattern recognition.

Annupan Rodtook received the M.Sc. in Computer Science from King Mongkut's Institute of Technology Ladkrabang of Thailand in 1996. He has received his Ph.D. degree in Technology from Sirindhorn International Institute of Technology, Thammasat University of Thailand in 2005. He is currently Assistant Professor at the Computer Science Department, Ramkhamhaeng University of Thailand. His research interests include image processing, medical image processing and pattern recognition.

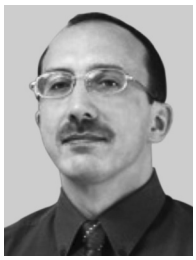

Stanislav S. Makhanov received the M.Sc. in Applied Mathematics from Moscow State University in 1981 and the Dr.Sc. from Computing Center of the Russian Academy of Science in 1988, where he worked as Associate Professor until 1993. From 1994 until 1999 he was a Visiting Professor with King Mongkut's Institute of Technology, Ladkrabang of Thailand and Associated Faculty with Asian Institute of Technology. He is currently Associate Professor with Sirindhorn International Institute of Technology, Thammasat University of Thailand. He is teaching courses in Applied Mathematics and Computer Science. Dr. Makhanov has published more than 100 research papers and conference proceedings in numerical methods and applications in robotics and image processing. He has been a consultant to UN (ESCAP) and other international organizations. Dr. Makhanov's biography has been published by Who is Who in Asia-2007, Who is Who in Science and Engineering-2008 and Who is Who in the World-2005, 2009.